

ELEMENT DISTRIBUTIONS IN THE CRAB NEBULA ¹

Timothy J. Satterfield, Andrea M. Katz, Adam R. Sibley, and Gordon M. MacAlpine

Department of Physics and Astronomy, Trinity University, San Antonio, TX 78212

and

Alan Uomoto

Carnegie Institution for Science, The Observatories, Pasadena, CA 91101

ABSTRACT

Images of the Crab Nebula have been obtained through custom interference filters which transmit emission from the expanding supernova remnant in He II $\lambda 4686$, $H\beta$, He I $\lambda 5876$, [O I] $\lambda\lambda 6300, 6364$, [N II] $\lambda\lambda 6548, 6583$, [S II] $\lambda\lambda 6716, 6731$, [S III] $\lambda 9069$, and [C I] $\lambda\lambda 9823, 9850$. We present both raw and flux-calibrated emission-line images. Arrays of 19,440 photoionization models, with extensive input abundance ranges, were matched pixel by pixel to the calibrated data in order to derive corresponding element abundance or mass-fraction distributions for helium, carbon, nitrogen, oxygen, and sulfur. These maps show distinctive structure, and they illustrate regions of gas in which various stages of nucleosynthesis have apparently occurred, including the CNO-cycle, helium-burning, carbon-burning, and oxygen-burning. It is hoped that the calibrated observations and chemical abundance distribution maps will be useful for developing a better understanding of the precursor star evolution and the supernova explosive process.

Subject headings: ISM: individual (Crab Nebula)—nuclear reactions, nucleosynthesis, abundances—supernovae: individual (SN 1054)—supernova remnants

¹This paper involves data obtained at the MDM Observatory and at the McDonald Observatory of The University of Texas at Austin.

1. Introduction

The Crab Nebula (M1 = NGC1952) is the visible remnant of the core-collapse supernova SN1054. Based on evidence from chemical processing in the line-emitting gas, MacAlpine & Satterfield (2008, herein MS) deduced an initial precursor star mass $\gtrsim 9.5 M_{\odot}$, and Wanaajo et al. (2009) have suggested that a $\sim 10 M_{\odot}$ precursor underwent an O-Ne-Mg core collapse to form the neutron star (PSR B0531+21) near the center of the nebula. The visible emitting gas and neutron star have a combined mass of at least several M_{\odot} (MacAlpine & Uomoto 1991), whereas the outer layers of the precursor may have been expelled in a presupernova wind (Nomoto et al. 1982) or a shockwave (Chevalier 1977). Major components of the visible nebula are synchrotron continuum emission produced by the pulsar wind and thermal line emission of material ejected from the interior of the precursor star. The expelled thermal gas, moving outwards with speeds up to about 1700 km s^{-1} (e.g., MacAlpine et al. 1996), is ionized and heated primarily by the synchrotron radiation field. The complex observed filamentary structure is characterized by a range of nuclear processing (MacAlpine et al. 2007, MS). Comprehensive reviews of the Crab Nebula have been prepared by Davidson & Fesen (1985) and Hester (2008), and a useful discussion of element abundances was previously given by Henry (1986).

The Crab Nebula is particularly well suited for investigating nucleosynthesis processes and explosion details for a relatively low-mass core-collapse supernova. Its age (as observed) and location out of the Galactic plane suggest that the ejecta are not heavily contaminated by swept-up interstellar material. Furthermore, numerous measured electron temperatures in the range 7,000-18,000 K (e.g., Woltjer 1958, Miller 1978, Fesen & Kirshner 1982, MacAlpine et al. 1989, 1996, and Satterfield 2010) imply that the line-emitting gas can be usefully analyzed in terms of ionization, temperature, and chemical abundances using powerful photoionization codes. Early photoionization modeling endeavors (e.g., Henry & MacAlpine 1982, Pequignot & Dennefeld 1983) were reasonably successful at matching observed line intensities and theoretical gas conditions for individual filaments. However, there were notable problems. For instance, observed [N II] $\lambda\lambda 6548, 6583$ from some of the gas was weaker than expected (see Wheeler 1978). Also, [C I] $\lambda\lambda 9823, 9850$ emission as measured at a number of locations (e.g., Henry et al. 1984) was stronger than computationally predicted for reasonable carbon abundance.

Regarding the [N II] problem, MacAlpine et al. (1996) employed long-slit spectroscopy, distributed over the nebula, to show that there is a range of nitrogen emission from the gas, including regions with high implied nitrogen abundance as necessitated by CNO processing of H into He. In addition, that study reported nebular locations with low nitrogen and high sulfur abundances, suggestive of further processing including oxygen-burning. In a more

comprehensive investigation, MacAlpine et al. (2007) used optical and near-infrared long-slit spectroscopy to measure and correlate numerous emission lines at many locations in the nebula in order to obtain a better understanding of the overall range of nuclear processing, from the CNO cycle through helium-burning and nitrogen depletion, to extensive regions containing enriched products of oxygen-burning. Then MS developed new photoionization calculations that do a better job of representing these various expected and observed stages of nuclear processing. The improved theoretical models also produce the observed [N II] and [C I] lines for reasonable nitrogen and carbon abundances.

The next step in our on-going investigation of chemical abundances and nuclear processing in the Crab Nebula is to map the overall distributions of elements like helium, carbon, nitrogen, oxygen, and sulfur. In this paper, we present new, flux-calibrated emission-line images obtained through custom-designed interference filters and also element mass-fraction (abundance) maps that result from matching pixel-by-pixel line fluxes with thousands of photoionization model calculations involving nested ranges of input abundances. Much of this work was carried out as part of the undergraduate honors theses of Satterfield (2010) and Katz (2011).

2. Observations

During 2008 December 1-4, we imaged the Crab Nebula in He II $\lambda 4686$, $H\beta$, He I $\lambda 5876$, [O I] $\lambda\lambda 6300, 6364$, [N II] $\lambda\lambda 6548, 6583$ (including $H\alpha$, which was subsequently removed), [S II] $\lambda\lambda 6716, 6731$, and synchrotron continuum emission in roughly 10-nm bandpasses centered at 5450 and 8050 Å. This was accomplished using the 2.7-m Harlan J. Smith Telescope at the McDonald Observatory, with the IGI imaging system and a 1024×1024 TK4 CCD. In addition, during 2009 December 18-21, we used the 1.3-m McGraw-Hill Telescope at the MDM Observatory, with the 2048×2048 Echelle CCD in direct mode, to image $H\beta$, [S III] $\lambda 9069$, [C I] $\lambda\lambda 9823, 9850$, and the aforementioned continuum bands in the nebula. Additional direct-mode imaging was necessitated in the near-infrared because of glass in the IGI camera at McDonald. In all cases, the radiation was imaged through custom designed interference filters manufactured by Omega Optical. The filters, with transmission curves shown in Figure 1, were designed to transmit emission lines or their multiplets from gas expanding outwards at speeds up to 1700 km s⁻¹. In addition, at least two calibrated standard stars (selected from Feige 34, Feige 110, G191-B2B, G158-100, and Hiltner 600) were observed through each filter.

2.1. Initial Calibrations

All images were bias-level subtracted using overscan regions and combined zero-second exposures, as accomplished with the *ccdproc* routine in the IRAF (Tody 1986) software package. The optical images were flat-field corrected with the aid of dome flats, while the near-infrared images were corrected for both flatness and fringing using sky flats. Then all of the images were carefully registered to coincide with the Crab Nebula Fabry-Perot datacube of Lawrence et al. (1995) (for reasons to be discussed later) using the *geomap* and *geotran* IRAF routines. Because of variable seeing and the fact that images would ultimately be directly compared with each other on a pixel-to-pixel basis, it was also necessary to “degrade” them to be consistent with the poorest seeing case, using *psfmatch* so stars would all have the same point-spread functions. Ultimately, we were able to median combine the multiple exposures for each image without loss of data, with each pixel effectively representing the same gas in the different images. Resultant “raw” combined images are shown in Figures 2 and 3.

2.2. Sensitivity and Flux Calibrations

Next, we determined the system sensitivity for each filter and calibrated each image in terms of $\text{ergs cm}^{-2} \text{s}^{-1} \text{pixel}^{-1}$. Accurate and consistent sensitivity values were derived from the observed standard stars at the McDonald Observatory, but the standard star results were not sufficiently consistent in the MDM Observatory observations due to variable sky conditions. Therefore, in the latter cases, we used the pulsar’s known energy distribution (Sollerman et al. 2000) for this purpose.

To obtain the system sensitivity, we followed a method similar to that described by Jacoby et al. (1987). Neglecting atmospheric absorption initially, the total flux ($\text{ergs cm}^{-2} \text{s}^{-1}$) from a standard star, S , incident on the detector, through filter i , can be characterized by

$$F_S(i) = \int F_{S\lambda} T_\lambda(i) d\lambda$$

which convolves $F_{S\lambda}$ ($\text{ergs cm}^{-2} \text{s}^{-1} \text{\AA}^{-1}$) of each standard star above the atmosphere with each filter’s transmission curve, $T_\lambda(i)$. Then we can define a “system sensitivity” for each filter, taking into account atmospheric absorption, telescope optics, and detector response as

$$S(i) = F_S(i) / [C_S(i) \times 10^{0.4kA(i)}]$$

where $C_S(i)$ represents the observed star count rate and k is the appropriate airmass extinction coefficient (Massey & Foltz 2000) in magnitudes per airmass $A(i)$.

Assuming uniformly distributed continuum emission across filter transmission bands, we can represent the measured continuum flux in any pixel with

$$F_C(i) = \langle S(i) \rangle C_C(i) \times 10^{0.4kA(i)} / \langle T_\lambda(i) \rangle$$

where $\langle S(i) \rangle$ may be an average from several standard stars, C_C is the continuum count rate for the bandpass and $\langle T_\lambda(i) \rangle$ represents the effective average transmission for a filter.

Dealing with the line emission is more complicated. For each pixel, and a given filter, there may be multiple contributions from gas with different line-of-sight velocities and therefore different wavelength shifts distributed over the filter transmission curve. As seen in Figure 1, the transmission curves are not perfectly uniform over the wavelength ranges where line emission may arrive. Assuming various emission lines have similar line-of-sight velocity distributions, we employed the Crab Nebula [O III]-emission Fabry-Perot datacube of Lawrence et al. (1995) to address this issue. As discussed previously, all of our images have been modified to the same resolution and registered to this 27-image datacube, which we used to produce an appropriately-weighted wavelength distribution for line emission at each pixel. Then, for the line flux at each pixel, through a given filter i ,

$$F_L(i) = \langle S(i) \rangle C_L(i) \times 10^{0.4kA(i)} \sum [w_\lambda / T_\lambda(i)]$$

where $\sum [w_\lambda / T_\lambda(i)]$ is the transmission weighted sum. For any pixels where [O III] emission in the Fabry-Perot datacube was not sufficient to yield reliable weighting factors, the line flux was computed in a manner similar to that for the continuum, effectively centering the line in the filter bandpass.

2.3. Sky and Continuum Subtraction

The flux-calibrated images (in $\text{ergs cm}^{-2} \text{ s}^{-1} \text{ pixel}^{-1}$) still contained contributions from both the background sky and synchrotron continuum. To remove the former, we subtracted the average of numerous 300×300 pixel areas in different directions and well outside the visible nebulosity. Then, to ensure consistency and mitigate signal-to-noise issues in the rest of the reduction process, we zeroed out any pixel with a value lower than three times the remaining background's standard deviation above its average of zero.

For a given emission-line image, the closer in wavelength of the continuum images was used for removal of the overlying synchrotron radiation. To facilitate this process in an

objective and consistent way, we carefully identified the same regions in all images, devoid of line emission within the central part of the nebula; and we subtracted the appropriate continuum image down to the previously-measured three standard deviations above the background average of zero.

Flux-calibrated and continuum-subtracted images are shown in Figures 4 and 5. Because the filter that isolated light in [N II] $\lambda\lambda 6548, 6583$ also transmitted $H\alpha$ $\lambda 6563$, our calibrated $H\beta$ image was scaled by a factor of 2.85 and subtracted from the [N II] image in order to remove contributions from $H\alpha$. Also, as discussed by Davidson et al. (1982) and by Blair et al. (1992), He II $\lambda 4686$ emission may arise in more diffuse gas compared with that producing other lines being considered here, so images for that line in Figures 2 and 4 are presented as observational data only and will not be used for further comparative abundance analyses in this paper.

2.4. Ratios of Emission Lines to $H\beta$

To facilitate comparisons of our observed emission-line fluxes with output from the numerical photoionization code Cloudy (Ferland et al. 1998), we could deal directly with the fluxes and then ratio results for different elements in order to derive relative abundances, or we could normalize initially by dividing each line image by the $H\beta$ image and then compare the observations with *relative* line intensities from the models. We chose the latter approach. Before creating the images for lines/ $H\beta$, we reassigned an arbitrarily large number (10^6) to each zero-valued $H\beta$ pixel as well as to each pixel with a flux value less than 10^{-16} ergs cm $^{-2}$ s $^{-1}$. This eliminated the potential for infinite ratio values and for boosting by more than a factor of ten resulting from division by $H\beta$. The flux ratio images, corrected for interstellar reddening according to $E_{B-V} = 0.47$ and $R = 3.1$ (see Davidson & Fesen 1985), are presented in Figure 6.

3. Element Mass Fraction Distributions

Element mass-fraction maps were produced by comparing the observational flux ratio distributions of Figure 6 with a grid of 19,440 Cloudy code models involving nested element abundances (to be discussed below). We developed algorithms that interact with the code output of computed emission-line ratios and identify the model with the “optimal-fit” abundances for each image pixel. Before elaborating further on this procedure and showing results, we consider some caveats to keep in mind for computations of this type applied to

the Crab Nebula.

3.1. Potential Complicating Factors

The photoionization code assumes ionization and thermal equilibrium for the line-emitting gas, whereas some particularly low-electron-density regions in the Crab Nebula may not have had time to achieve equilibrium during the observed lifetime of the remnant (see Davidson & Tucker 1970). On the other hand, the only emission considered here that may be significantly affected in this regard is [O I] $\lambda\lambda 6300,6364$, and even these lines are produced in gas with recombination times roughly a sixth of the observed age of the nebula. All the other lines under consideration develop in gas with high enough electron density for equilibrium to be reasonably assured (MS).

In addition, as first emphasized by Davidson (1973), line-emitting gas in the Crab Nebula may be immersed in synchrotron radiation approaching from all directions, whereas the Cloudy code is used in a manner more appropriate for ionizing radiation from one direction. To consider this, MS developed algorithms for converting plane-parallel results to what could be expected for convex cylindrical and spherical clouds in the synchrotron nebula. Changes of 30-40% could result for computed [S II] $\lambda\lambda 6716,6731/H\beta$ or [O I] $\lambda\lambda 6300,6364/H\beta$ in the most extreme cases of going from plane-parallel to spherical geometries. Although we discuss below how this could affect our results, we believe it is reasonable to consider plane-parallel geometries in the current investigations of large-scale element distributions.

Other potential complicating issues involve assumptions about model input parameters such as ionizing radiation spectral characteristics, radiation flux striking a cloud, and gas density. As noted by Davidson & Fesen (1985), Hester (2008), and Charlebois et al. (2010), these conditions could vary spatially within the nebula. Furthermore, our emission-line imaging technique involving relatively broad-bandpass filters may lead to a variety of observed conditions along any line of sight. On the other hand, MS were able to use similar inputs for parameters in developing numerical models that gave reasonable matches to observational data for different regions in the Crab Nebula. For the present work, we tried to be as straightforward as possible in developing a necessarily fairly crude two-dimensional overall understanding of element distributions. We always used the input ionizing radiation spectrum adopted by MS, which is consistent with observations and essentially the same as suggested in the documentation that accompanies the Cloudy code. Furthermore, we did not vary the flux of ionizing radiation striking gas clouds. With regard to density considerations, we examined a number of significantly different potential paradigms, two of which we will discuss and compare here.

3.2. Matching Theoretical Models With Observed Pixels

For our assumptions regarding the radiation field and density, we developed a large grid of numerical photoionization simulations with extensive ranges of element abundances. The models were arranged in a nested hierarchy, beginning with six helium abundances, then six carbon abundances for each helium abundance, six nitrogens for each carbon, six oxygens for each nitrogen, and fifteen sulfurs for each oxygen ($2.5 \times 6^5 = 19,440$ models). Specifically, letting $\text{MF}(E)/\text{MF}(E)_\odot$ be a modeled element (E) mass fraction compared with its solar value in the Cloudy code file, we considered $\text{MF}(\text{He})/\text{MF}(\text{He})_\odot = 1.9, 2.8, 4.8, 9.8, 21, \text{ and } 33$. For each helium value, we let $\text{MF}(\text{C})/\text{MF}(\text{C})_\odot = 1.0, 6.0, 13, 19, 25, \text{ and } 31$. Then for each carbon value, $\text{MF}(\text{N})/\text{MF}(\text{N})_\odot = 0.1, 1.0, 1.9, 2.8, 3.7, \text{ and } 4.6$. For each nitrogen value, $\text{MF}(\text{O})/\text{MF}(\text{O})_\odot = 1.0, 7.0, 13, 20, 26, \text{ and } 31$. Finally, for each oxygen value, $\text{MF}(\text{S})/\text{MF}(\text{S})_\odot = 1.0, 2.0, 3.0, 4.0, 5.0, 6.0, 7.0, 8.0, 9.0, 10, 11, 12, 13, 14, \text{ and } 15$. We used a finer abundance grid for sulfur for reasons to be discussed below.

In the Cloudy code, input abundances for each element (E) were specified as scale factors

$$n = [N(E)/N(H)]/[N(E)/N(H)]_\odot,$$

representing the number density compared with hydrogen divided by the solar number density compared with hydrogen. To derive n for each $\text{MF}(E)/\text{MF}(E)_\odot$ above, it may be shown that

$$n = [\text{MF}(E)/\text{MF}(E)_\odot][\text{MF}(H)_\odot/\text{MF}(H)],$$

where we let $[\text{MF}(H)_\odot/\text{MF}(H)] = 0.7/[1 - \text{MF}(\text{He}) - \text{MF}(\text{heavier elements})]$.

For a given element, the total mass-fraction range considered was adopted by comparing models with observations, and there is correspondence with theoretical mass fractions to be expected in the core of an evolved $10 M_\odot$ star (see Woosley & Heger 2007). We did not actually consider the highest possible mass fractions suggested by the stellar models because computed line-emission ratios became less sensitive to changes above our upper abundance cutoffs. Other related element abundances were also varied as appropriate; for instance, silicon and argon mass-fractions followed those of sulfur, since they are all produced from oxygen-burning. Computed line intensities were extracted from the models at a distance into a cloud of three times the so-called Strömgren length at which half the atomic hydrogen is ionized; and it was found that gas deeper into a cloud does not contribute substantially more line emission.

In order to find optimal matches to imaged pixels from among the 19,440 abundance models, we considered several different approaches, ultimately adopting one that matches helium first, rather than giving equal weight to all elements simultaneously. This took into

account helium’s importance for physical conditions like the ionization structure. For each pixel (representing the same nebular gas for all images; see § 2.1), a numerical algorithm was used to select the subset of 19,440/6 models with a helium abundance (from the six considered) most closely matching the observed He I $\lambda 5876/H\beta$ ratio. From those models, the smaller subset of 19,440/36 models with carbon abundance most closely matching observed [C I] $\lambda\lambda 9823, 9850/H\beta$ was selected, followed by similar procedures for nitrogen, oxygen, and sulfur (involving only 15 models in the last case). Ultimately, one computed model was identified as having abundances most closely representing each image pixel.

The computed and observed line ratios, as matched for initially establishing abundances at each pixel, had average residuals of 10-38% compared with the measurements. However, the ultimately selected abundance model for each pixel will not necessarily have the same lines that were matched to set up the abundances. For instance, once a helium abundance is initially selected, there are 19,440/6 or 3,240 models for that abundance, any of which could ultimately represent the pixel, depending on line matches and abundances for the other elements. On the other hand, it was reassuring that the helium line residuals for the *final* models of all the pixels averaged only 23% compared with the observations.

While investigating details of the matching process, it was noted that, for some circumstances, the computed [S II] $\lambda\lambda 6716, 6731/H\beta$ ratio first increased with rising sulfur mass fractions up to about 6-8 times solar, and then flattened or even decreased somewhat. The latter situation could lead to redundancy for some pixels, whereby their matched observed and theoretical line ratios might correspond with either high or low sulfur abundance. Experimentation showed that this potential double-value dilemma is more likely to occur with lower helium abundances (due to effects on ionization structure) and for lower hydrogen densities. Plotting of temperature, density, and line emissivity suggests it is a temperature effect, whereby increasing the modeled sulfur and silicon abundances results in more collisional cooling, partly from the fine-structure [S III] and [Si II] transitions discussed by Henry (1993). As the sulfur mass fraction increases and the gas temperature goes down, the [S II]/ $H\beta$ ratio first increases because of more S^+ and then declines because of relative temperature dependences of [S II] and $H\beta$ emission. To deal with this dilemma, we used a finer abundance grid for sulfur (fifteen abundances rather than six as for other elements); and our algorithm that matches models with observations was set to flag any potential double-valued pixels and to select the lower abundance if two are possible for an observation. The problem is significantly less important for [S III] $\lambda 9069$ emission. Whereas the [S II] and [S III] lines lead to similar sulfur abundance spatial distributions, [S III] emission yields regions with higher sulfur content (places where the [S II] algorithm detected two abundance possibilities and selected the lower one). Because of this situation, *sulfur abundance maps derived from [S III] emission should be considered as more realistic*. Although other element abundances

were derived from models with a range of sulfur and silicon content, their mass-fraction maps were not significantly affected by this problem.

It could be useful to test the validity of the pixel-model matching process by comparing our theoretical computations with published spectroscopic measurements for *multiple* ionization stages of oxygen at various positions. Unfortunately, this becomes seriously complicated when trying to match spectroscopic slits or apertures with our image pixels and also when considering imaged emitting gas with different velocities along the line of sight. Our best opportunity for this type of test may be position 8 of Fesen & Kirshner (1982), which appears to be relatively well defined with a dominant single-velocity spectrum. Our models averaged over four pixels at that location give [O II] $\lambda 3727/\text{H}\beta = 11.83$ (compared with 14.90 measured by Fesen & Kirshner) and [O III] $\lambda 5007/\text{H}\beta = 7.66$ (compared with 9.82 measured by Fesen & Kirshner). The residuals are consistent with the averages found above from matching our model outputs with our imaged lines.

Carbon also provides observed lines representative of multiple ionization stages, namely [C I] $\lambda\lambda 9823, 9850$ as imaged and modeled here and also C III] $\lambda 1909$ and C IV $\lambda 1549$ in the ultraviolet. However, as discussed by Davidson (1978), Davidson et al. (1982), Henry & MacAlpine (1982), and Blair et al. (1992), much of this ultraviolet line emission probably comes from lower-density, more diffuse gas, compared with the bright optical-line-emitting condensations being considered here.

As noted previously, for this investigation we will examine two sets of photoionization model simulations, with different assumptions regarding gas density input parameters. The first models are similar to those of MS, with constant hydrogen density of $3,000 \text{ cm}^{-3}$ and constant $\log U = -3.5$ (where the so-called ionization parameter, U , is defined for the Cloudy code as Φ/cN , or the flux of hydrogen ionizing photons striking a cloud divided by the speed of light times the hydrogen density). With these assumptions, the total nuclear density can be higher by as much as a factor of 4-5 for regions with very high helium abundances, but this is well within the density variation range suggested by Jun (1998). The second grid of models is characterized by *constant nuclear density* of $6,000 \text{ cm}^{-3}$, resulting in a range of 4-5 for hydrogen density as the helium abundance varies. Since both types of simulations assume the same ionizing radiation flux, the second set also involves appropriately varying ionization parameters. The specific density values in each case were considered because they produce similar electron-density-dependent [O II] $\lambda 3726/\lambda 3729$ ratios, which are consistent with observations (e.g., Fesen & Kirshner 1982).

3.3. Mass-Fraction Plots

The resultant element abundance plots for the two density paradigm cases described above are shown in Figures 7 and 8. Helium is presented in terms of its overall mass percentage in the emitting gas, whereas other elements are given as rough multiples of their solar mass fractions.

We note that the helium mass fraction maps are virtually indistinguishable for the two input density regimes. Helium comprises about 40% to >90% of the emitting gas in different regions, with an overall derived distribution very much like that reported by Uomoto & MacAlpine (1987). There is an area with relatively low helium in the north, possibly indicative of an ambient interstellar cloud (Morrison & Roberts 1985, Fesen & Gull 1986). In addition, the roughly east-west high-helium band or torus (see also Lawrence et al. 1995) stands out as a prominent feature.

For the two types of models illustrated, the carbon, nitrogen, and oxygen mass-fraction maps are similar in terms of overall structure, with some quantitative differences especially for carbon. On the other hand, the sulfur maps show some notable variation. As discussed previously, double valuing tends to occur for matching [S II]/ $H\beta$ emission and sulfur abundance, resulting in the lower possible abundance being selected by our algorithm. Therefore, the sulfur maps derived from [S II] emission show some unrealistically low mass-fractions. We do not know which (if either) set of input density assumptions is more appropriate for Crab Nebula emitting gas, and we will *arbitrarily* concentrate on the constant nuclear density maps (Fig. 8) in further discussion below.

Next, we consider carbon, which is a product of helium fusion. The distribution map of Figure 8(b) shows a wide range of carbon mass fraction, from roughly solar to more than 30 times solar. This is consistent with the results of MS, who demonstrated how the strong observed [C I] $\lambda\lambda 9823, 9850$ doublet arises from electron collisional excitation in gas with very high helium abundance and who then used spectroscopic measures along with photoionization simulations to derive carbon concentrations more than 10 times solar in parts of the Crab Nebula. As shown by the ionization, temperature, and density diagrams in Figures 2-5 of MS, very high helium abundance causes rapid depletion, near the face of a cloud, of ionizing photons with energy above 24.6 eV, the ionization potential of He^0 . Because C^+ has a comparable ionization potential and that for C^0 is below 13.6 eV, the dominant ionization stage for carbon is C^+ . Recombination of C^+ to C^0 in the warm He^0 and H^+ zone leads to strong collisionally-excited [C I] $\lambda\lambda 9823, 9850$ emission, which becomes more pronounced for higher helium abundance as illustrated in Figure 9 (from Katz 2011).

We note that the carbon mass-fraction distribution does not exactly follow the observed

[C I] flux of Figure 5(h) or the [C I]/H β map of Figure 6(f). This can be understood from examination of the helium distribution in Figure 8(a) and consideration of Figure 9. Regions with relatively lower [C I] emission and lower helium abundance may actually contain more carbon compared with regions of higher [C I] emission and higher helium abundance.

Helium abundance is not the only reason why [C I] $\lambda\lambda 9823, 9850$ emission is stronger in the Crab Nebula than in other types of astronomical objects. Because of effects on photon mean free paths and ionization transition zone widths, the ionization parameter and gas density can also play roles in producing this emission, as illustrated in Figure 10 (from Katz 2011). Planetary nebulae or H II regions may be characterized by gas with log U of order 0 (e.g., Becerra-Davila et al. 2001), so we would not expect strong [C I]/H α from them, even if the helium abundance were high. In addition, for expected densities of 10^6 cm^{-3} or higher, [C I] emission should not stand out in a Seyfert galaxy or quasar spectrum.

As shown in Figures 5(e) and 6(c), [N II] $\lambda\lambda 6548, 6583$ emission is strong in the northern part of the nebula, in accord with the long-slit spectroscopic findings of MacAlpine et al. (1996). Resultant derived elevated nitrogen abundances could have arisen from the CNO-cycle, with relatively low helium in that region indicative of interaction with an ambient cloud (see above). MS showed how high helium abundance is conducive to producing strong [N II] emission, so lower helium abundance in the north (see Figure 8(a)) also leads to higher derived nitrogen abundance for a measured [N II] intensity. According to Figure 8(c), the nitrogen abundance tends to be lower in those parts of the nebula where a lot of carbon exists, probably as a result of $^{14}\text{N}(\alpha, \gamma)^{18}\text{F}(\beta^- \nu)^{18}\text{O}(\alpha, \gamma)^{22}\text{Ne}$ processing which would be expected to accompany helium-burning (Nomoto 1985). Infrared neon lines have been measured in the Crab Nebula by Temim et al. (2006). They reported strong emission from [Ne II] $12.8 \mu\text{m}$ and [Ne III] $15.5 \mu\text{m}$ near the center of the nebula, where we find relatively low nitrogen abundance. Furthermore, MacAlpine et al. (2007) found an inverse relation between their measured [N II] $\lambda 6583$ and the Temim et al. measured [Ne II] $12.8 \mu\text{m}$ for a particular position. Finally, we note that the apparent high nitrogen abundance around some edges of the nebula may be real, or it could be due in part to our use of [N II]/H β ratios for regions with very weak H β emission (compare Figures 4(b), 5(e) and 6(c)).

Turning our attention now to the observed [O I] $\lambda\lambda 6300, 6364$ fluxes, [O I]/H β ratios, and oxygen mass-fraction distributions of Figures 4(d), 6(b), and 8(d), respectively, we see strong emission and high oxygen abundance in the central east-west band of the nebula, including in outlying parts of the high-helium torus region. Oxygen could arise from helium or carbon-burning. From examination of element overlaps (or lack thereof) in the Woosley & Heger (2007) $10 M_{\odot}$ stellar core mass-fraction diagram, it may seem odd that some of the highest oxygen abundances in Figure 8(d) appear to coincide with regions where the helium

abundance is also quite high. However, this apparent anomaly could result from gas mixing in the Crab Nebula or from a combination of different gas regimes along our line of sight. Mixing and averaging of emission along sight lines may also help to explain why we do not derive oxygen mass fractions as high as the maximum in the Woosley & Heger mass cut simulation. In addition, as noted in § 3.1 above, for [O I] emission, consideration of spherical geometry cloudlets immersed in the synchrotron radiation field could lead to a decrease of as much as 40% in the computed [O I]/ $H\beta$ ratio and to a corresponding increase in the derived oxygen mass fraction for a given pixel. Going to a cylindrical filamentary geometry would have somewhat less effect.

Finally, we consider the [S II] $\lambda\lambda 6716, 6731$ and [S III] $\lambda 9069$ emission in Figures 5(f), 5(g), 6(d), and 6(e), along with the [S III]-derived (see previous discussion) sulfur mass-fraction map of Figure 8(f). The general [S II] emission features are similar to those in MacAlpine et al. (1989) and Charlebois et al. (2009). The raw [S III] image here has less signal-to-noise, is more dominated by continuum, and shows fewer prominent features compared with the raw [S II] image. However, the flux-calibrated and continuum-subtracted images look very much alike. We note that [S III] $\lambda 9069$ was chosen for this investigation, rather than the stronger line at $\lambda 9531$ because of telluric water vapor absorption in the region of the latter (see Stevenson 1994, Vermeij et al. 2002, MacAlpine et al. 2007). As illustrated in Figure 8(f), high sulfur abundance regions tend to avoid some western parts of the nebula, being concentrated primarily to the east, as might be understood in terms of off-center oxygen ignition (see Woosley & Weaver 1986). The sulfur concentrations appear to avoid regions with the highest helium and oxygen abundances, instead occupying the apparent loop-like structures. Fairly high sulfur in the south-east edge filaments could be real, or it may result from weak $H\beta$ in the [S III]/ $H\beta$ ratios used for comparison with the model computations.

4. Summary

We have presented new raw and flux-calibrated, continuum-subtracted emission-line images of the Crab Nebula in He II $\lambda 4686$, $H\beta$, He I $\lambda 5876$, [O I] $\lambda\lambda 6300, 6364$, [N II] $\lambda\lambda 6548, 6583$, [S II] $\lambda\lambda 6716, 6731$, [S III] $\lambda 9069$, and [C I] $\lambda\lambda 9823, 9850$. Ratios of line images to $H\beta$ were compared with an extensive grid of photoionization simulations in order to derive element mass-fraction maps for helium, carbon, nitrogen, oxygen, and sulfur. These distributions should be considered as somewhat simplified approximations in the sense that plane-parallel geometry was assumed, along with global assumptions regarding ionizing radiation and gas physical conditions. It may be possible in future studies to divide the nebula into differ-

ent regions with separate assumptions, but we believe from considering various parametric schemes, that the results presented are representative of the Crab Nebula’s general characteristics. Although there has apparently been mixing physically as well as observationally along the line of sight, and also pulsar wind-driven material, the element distributions are distinct and informative. They illustrate regions of gas in which various stages of nucleosynthesis have occurred, including the CNO-cycle, helium-burning, carbon-burning, and oxygen-burning. It is hoped that the calibrated observations and chemical abundance distribution maps will be useful for developing a better understanding of the precursor star evolution and the supernova explosive process. Work currently underway will extend this investigation to derive actual *mass* distributions and estimates of overall masses for the various elements.

This work was supported by Trinity University and the endowed Charles A. Zilker Chair position. We also thank the staffs of the McDonald Observatory and the MDM Observatory for providing technical assistance.

REFERENCES

- Becerra-Davila, F., Binette, L., & Casassus, S. 2001, *RevMexAA*, 10, 33
- Blair, W. P., Long, K. S., Vancura, O., Bowers, C. W., Conger, S., Davidsen, A. F., Kriss, G. A., & Henry, R. B. C. 1992, *ApJ*, 399, 611
- Charlebois, M., Drissen, L., Bernier, A.-P., Grandmont, F., & Binette, L. 2010, *AJ*, 139, 2083
- Chevalier, R. A. 1977, in *Supernovae*, ed. D. N. Schramm (Dordrecht: Reidel), 53
- Davidson, K. 1973, *ApJ*, 186, 223
- Davidson, K. 1978, *ApJ*, 220, 177
- Davidson, K., & Fesen, R. A. 1985, *ARA&A*, 23, 119
- Davidson, K., Gull, T. R., Maran, S. P., Stecher, T. P., Fesen, R. A., Parise, R. A., Harvel, C. A., Kafatos, M., & Trimble, V. L. 1982, *ApJ*, 253, 696
- Davidson, K., & Tucker, W. 1970, *ApJ*, 161, 437
- Ferland, G. J., Korista, K. T., Verner, D. A., Ferguson, J. W., Kingdon, J. B., & Verner, E. M. 1998, *PASP*, 110, 761

- Fesen, R. A., & Gull, T. R. 1986, *ApJ*, 306, 259
- Fesen, R. A., & Kirshner, R. P. 1982, *ApJ*, 258, 1
- Henry, R. B. C. 1986, *PASP*, 98, 1044
- Henry, R. B. C. 1993, *MNRAS*, 261, 306
- Henry, R. B. C., & MacAlpine, G. M. 1982, *ApJ*, 258, 11
- Henry, R. B. C., MacAlpine, G. M., & Kirshner, R. P. 1984, *ApJ*, 278, 619
- Hester, J. J. 2008, *ARA&A*, 46, 127
- Jacoby, G. H., Quigley, R. J., & Africano, J. L. 1987, *PASP*, 99, 672
- Jun, B.-I. 1998, *ApJ*, 499, 282
- Katz, A. M. 2011, Undergraduate Honors Thesis, Trinity University, San Antonio, TX
- Lawrence, S. S., MacAlpine, G. M., Uomoto, A., Woodgate, B. E., Brown, L. W., Oliverson, R. J., Lowenthal, J. D., & Liu, C. 1995, *AJ*, 109, 2635
- MacAlpine, G. M., Ecklund, T. C., Lester, W. R., Vanderveer, S. J., & Strolger, L.-G. 2007, *AJ*, 133, 81
- MacAlpine, G. M., Lawrence, S. S., Sears, R. L., Sosin, M. S., & Henry, R. B. C. 1996, *ApJ*, 463, 650
- MacAlpine, G. M., McGaugh, S. S., Mazzarella, J. M., & Uomoto, A. 1989, *ApJ*, 342, 364
- MacAlpine, G. M., & Satterfield, T. J. 2008, *AJ*, 136, 2152 (MS)
- MacAlpine, G. M., & Uomoto, A. 1991, *AJ*, 102, 218
- Massey, P. & Foltz, C. B. 2000, *PASP*, 112, 566
- Miller, J. S. 1978, *ApJ*, 220, 490
- Morrison, P. & Roberts, D. 1985, *Nature*, 313, 661
- Nomoto, K. 1985, in *The Crab Nebula and Related Supernova Remnants*, ed. M. Kafatos & R. B. C. Henry (Cambridge: Cambridge University Press), 97
- Nomoto, K., Sparks, W. M., Fesen, R. A., Gull, T. R., Miyaji, S., & Sugimoto, D. 1982, *Nature*, 299, 803

- Pequignot, D., & Dennefeld, M. 1983, *A&A*, 120, 249
- Satterfield, T. J. 2010, Undergraduate Honors Thesis, Trinity University, San Antonio, TX
- Sollerman, J., Lundqvist, P., Lindler, D., Chevalier, R., Fransson, C., Gull, T., Pun, C., & Sonneborn, G. 2000, *ApJ*, 537, 861
- Stevenson, C. C. 1994, *MNRAS*, 267, 904
- Tody, D. 1986, “The IRAF Data Reduction and Analysis System” in *Proc. SPIE Instrumentation in Astronomy VI*, ed. D. L. Crawford, 627, 733
- Temim, T., et al. 2006, *AJ*, 132, 1610
- Uomoto, A., & MacAlpine, G. M. 1987, *AJ*, 93, 1511
- Vermeij, R., Damour, F., van der Hulst, J. M., & Baluteau, J.-P. 2002, *A&A*, 390, 649
- Wanajo, S., Nomoto, K., Janka, H.-T., Kitaura, F. S., & Muller, B. 2009, *ApJ*, 695, 208
- Wheeler, J. C. 1978, *ApJ*, 225, 212
- Woltjer, L. 1958, *Bull. Astron. Inst. Netherlands*, 14, 39
- Woosley, S. E. & Heger, A. 2007, *PhR*, 442, 269
- Woosley, S. E. & Weaver, T. A. 1986, in “Nucleosynthesis and Its Implications on Nuclear and Particle Physics,” ed. J. Audouze & N. Mathieu (Dordrecht: Reidel), 145

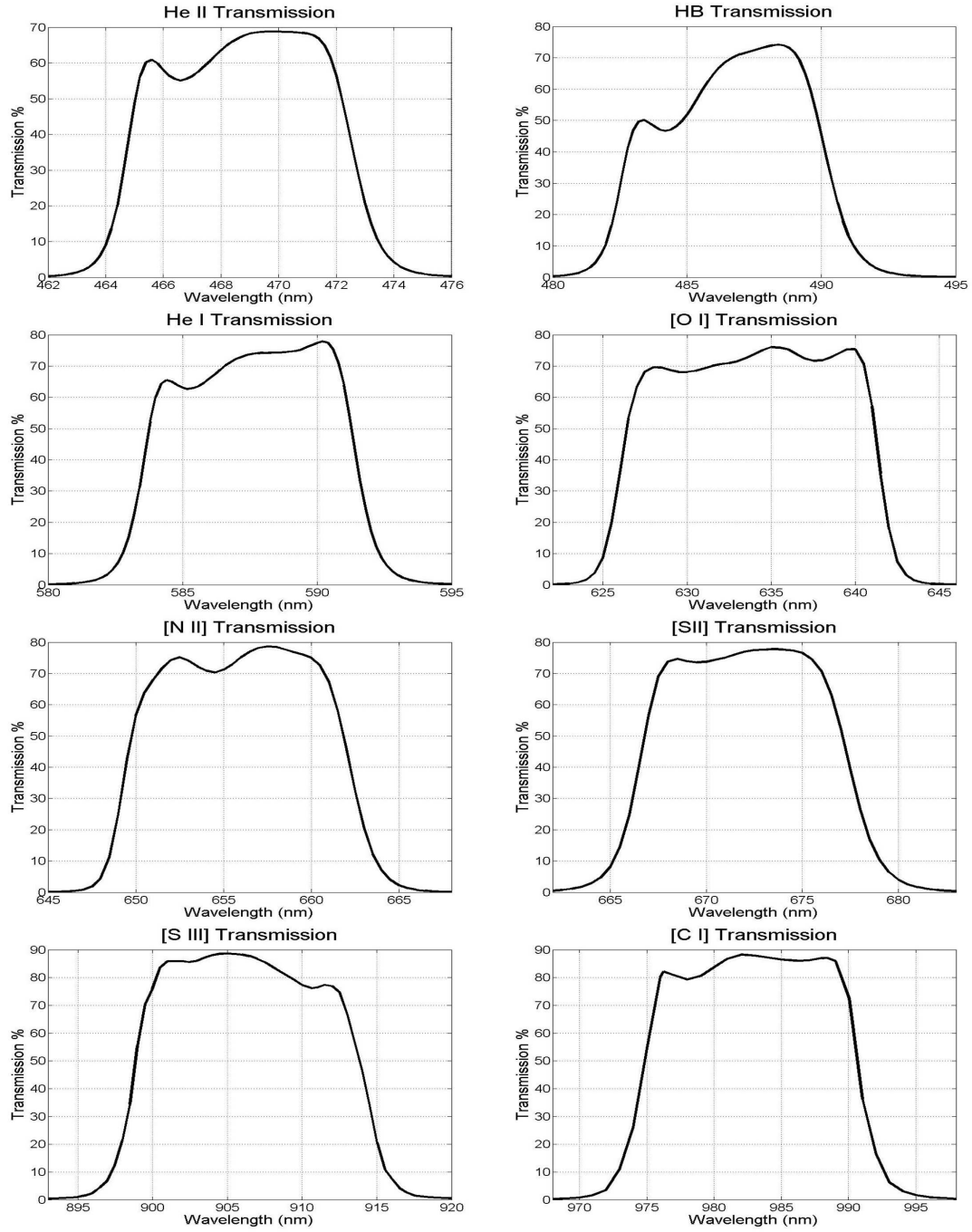


Fig. 1.— Filter transmission curves.

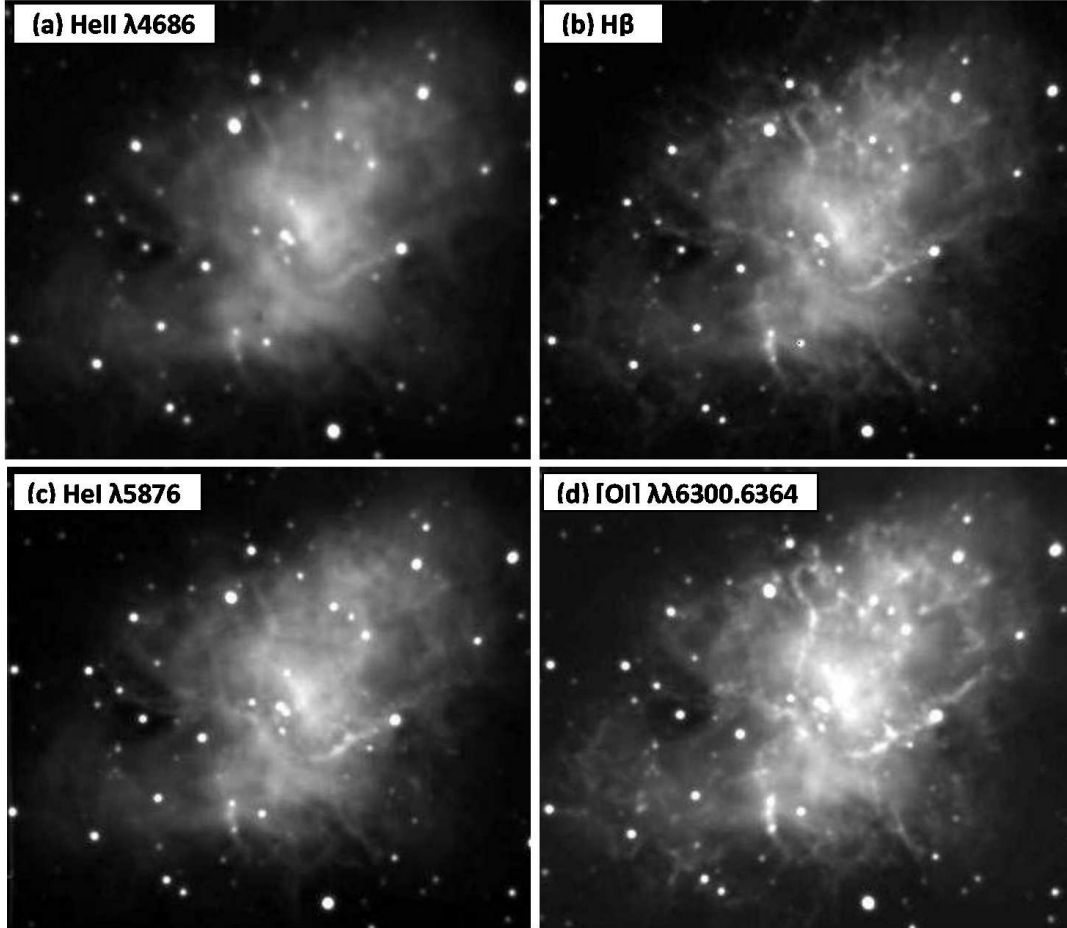


Fig. 2.— Raw emission-line images.

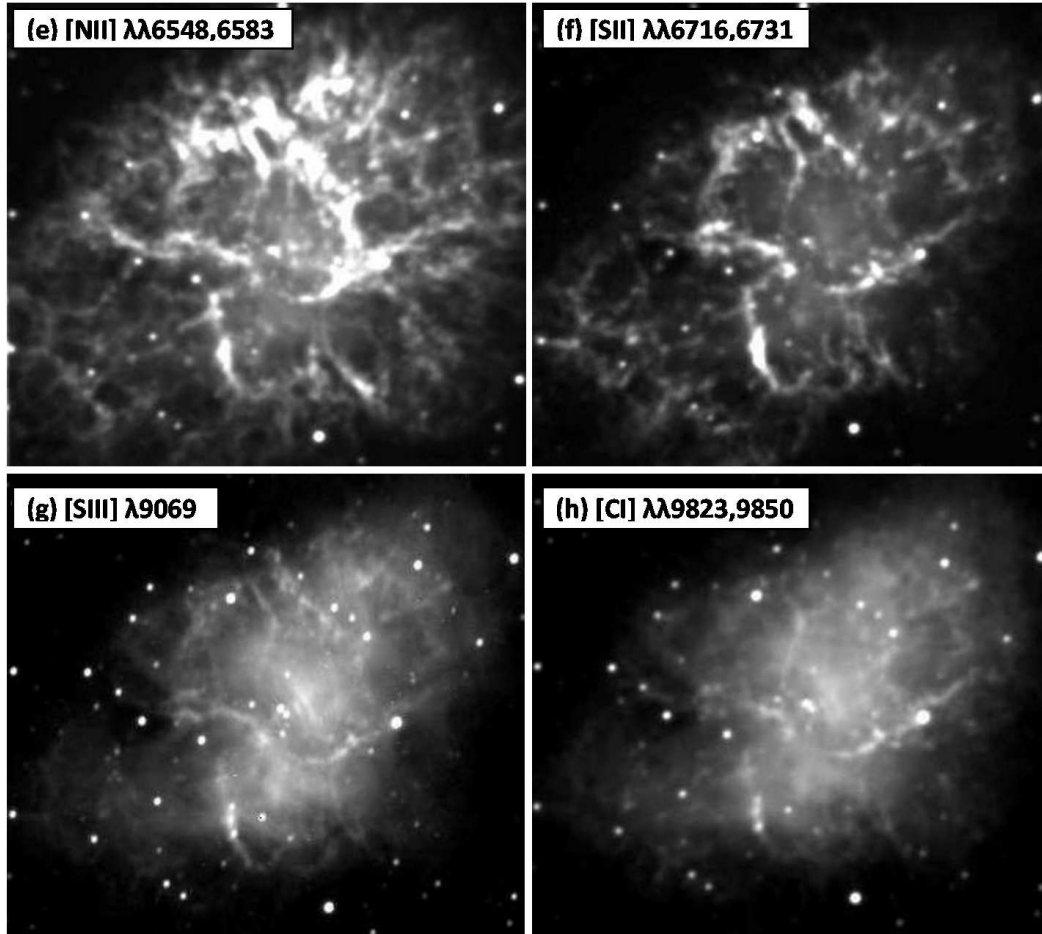


Fig. 3.— Raw emission-line images continued.

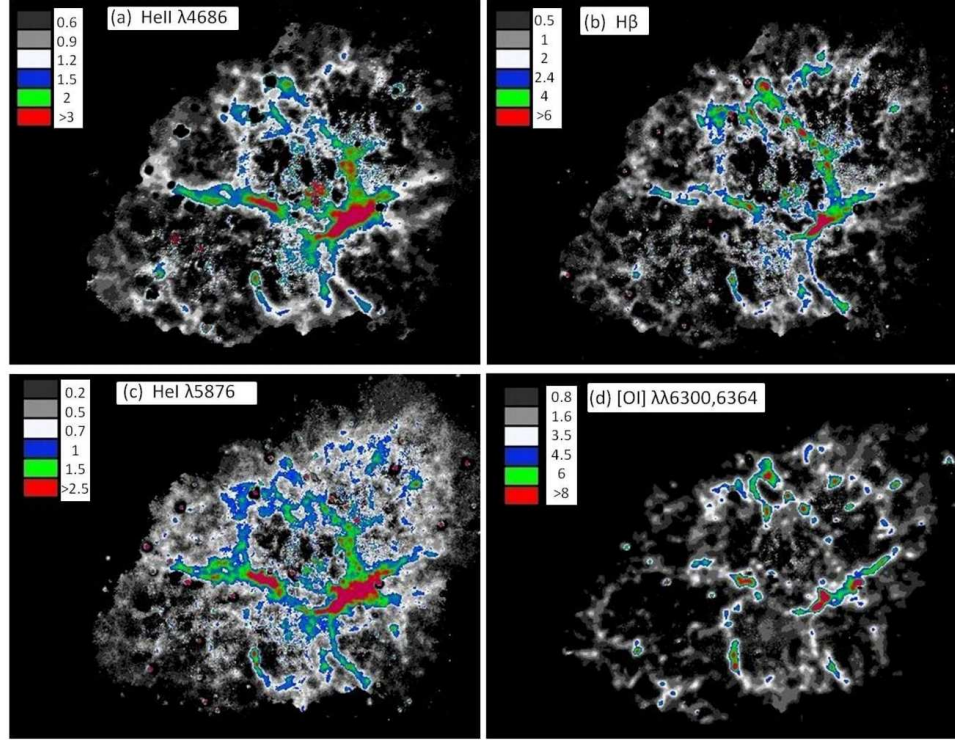


Fig. 4.— Flux-calibrated, continuum-subtracted emission-line images. Color coded fluxes are the numbers shown times $10^{-15} \text{ ergs cm}^{-2} \text{ s}^{-1}$.

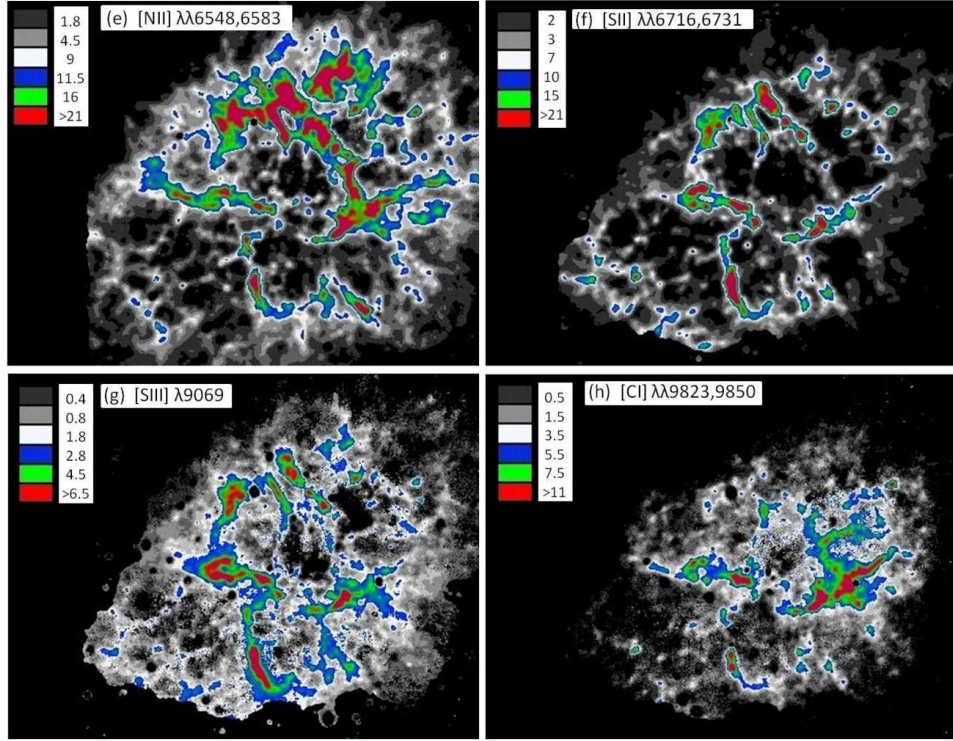


Fig. 5.— Flux-calibrated, continuum-subtracted emission-line images continued. Color coded fluxes are the numbers shown times $10^{-15} \text{ ergs cm}^{-2} \text{ s}^{-1}$.

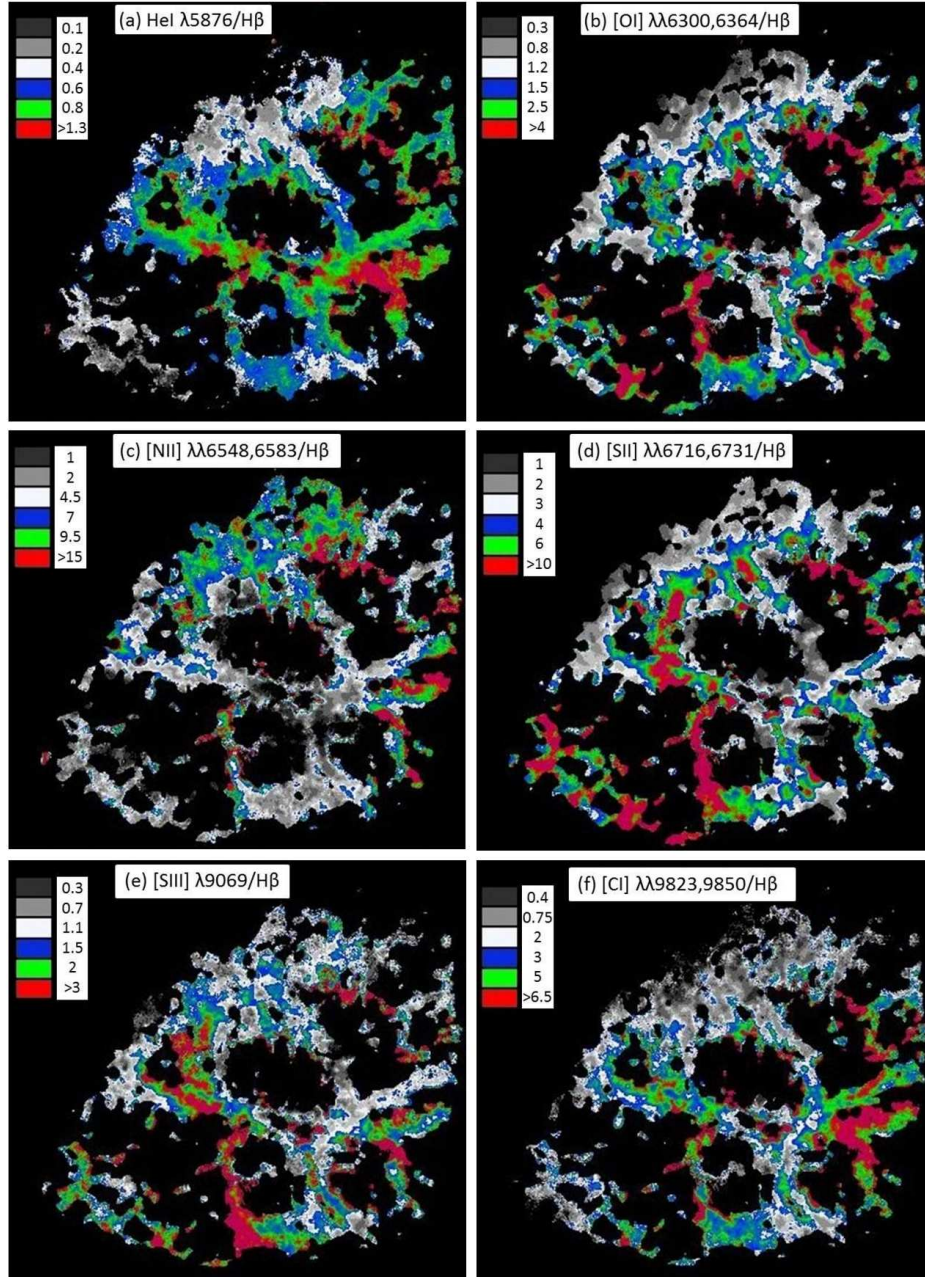


Fig. 6.— Ratios of emission-line images to the $H\beta$ image.

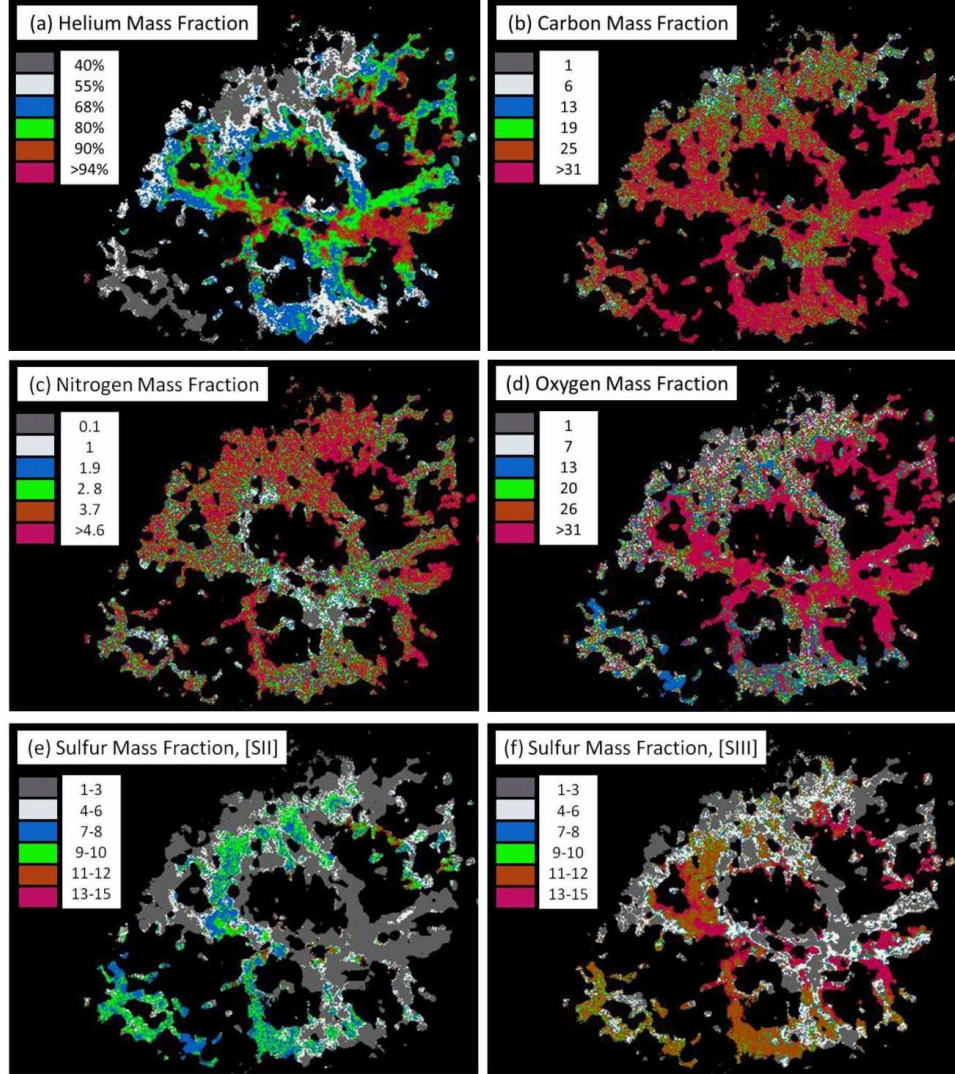


Fig. 7.— Computed mass-fraction distributions for constant hydrogen density and constant ionization parameter (see text). Helium mass fractions are specified as overall percentage of emitting-gas mass, whereas other elements are labeled as multiples of their solar mass fractions.

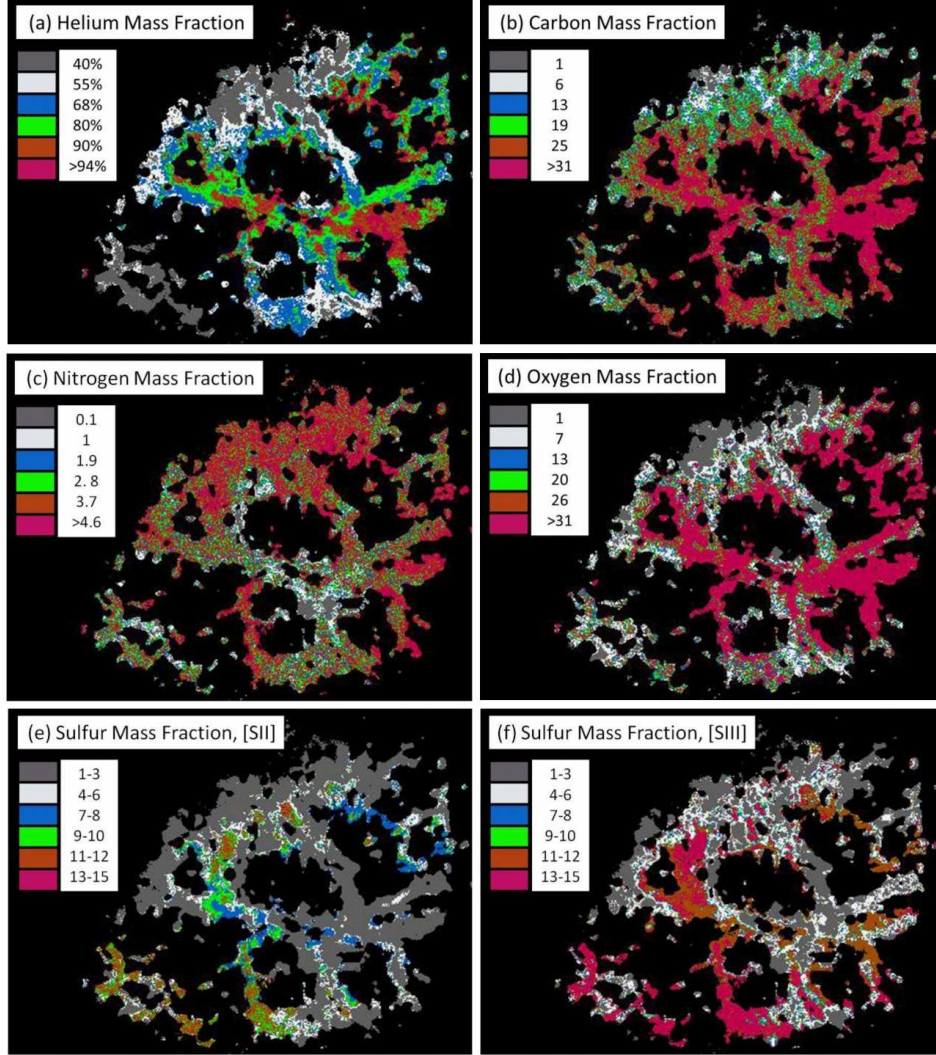


Fig. 8.— Computed mass-fraction distributions for constant overall nuclear density, with varying hydrogen density and ionization parameter (see text). Helium mass fractions are specified as overall percentage of emitting-gas mass, whereas other elements are labeled as multiples of their solar mass fractions.

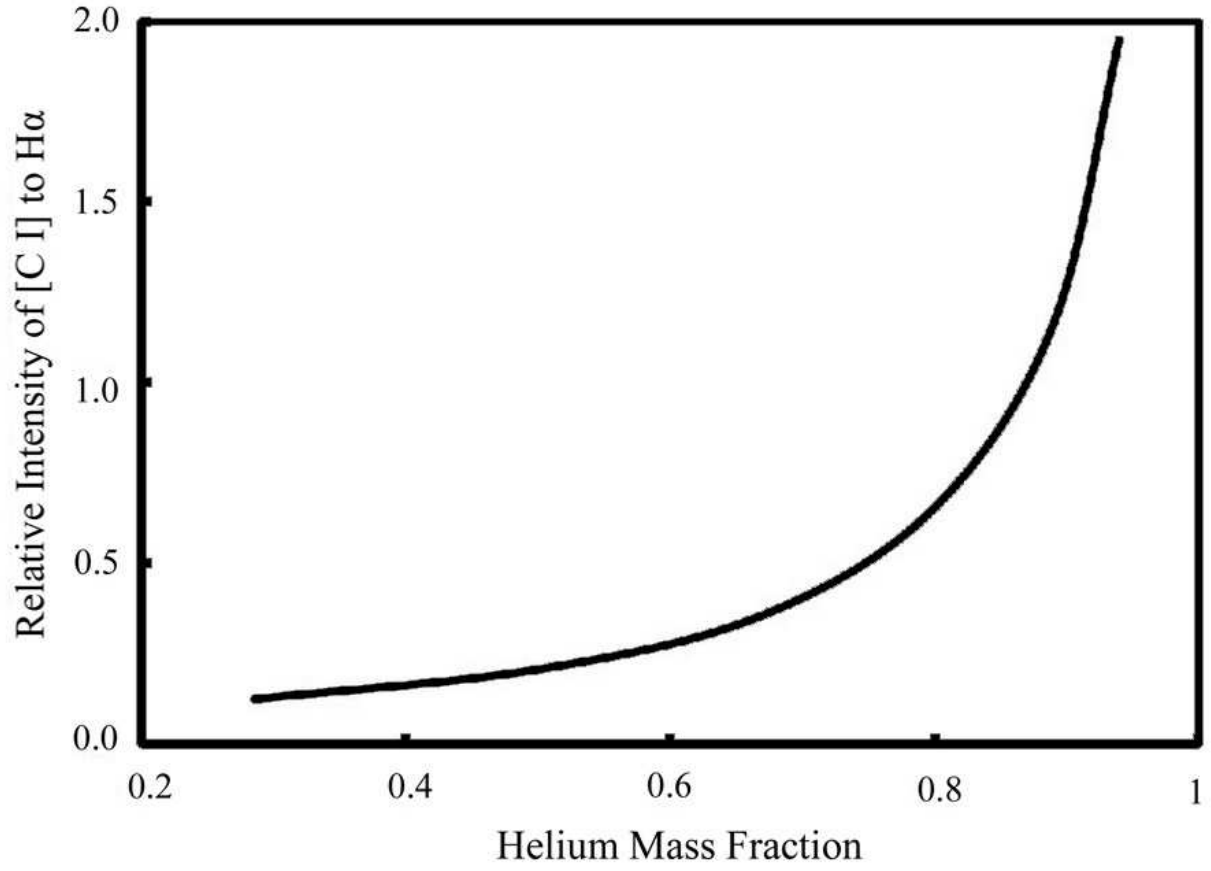


Fig. 9.— Computed [C I] $\lambda\lambda 9823,9850$ to $H\alpha$ ratio as a function of helium mass fraction. For hydrogen density= $3,000\text{ cm}^{-3}$ and $\log U=-3.5$.

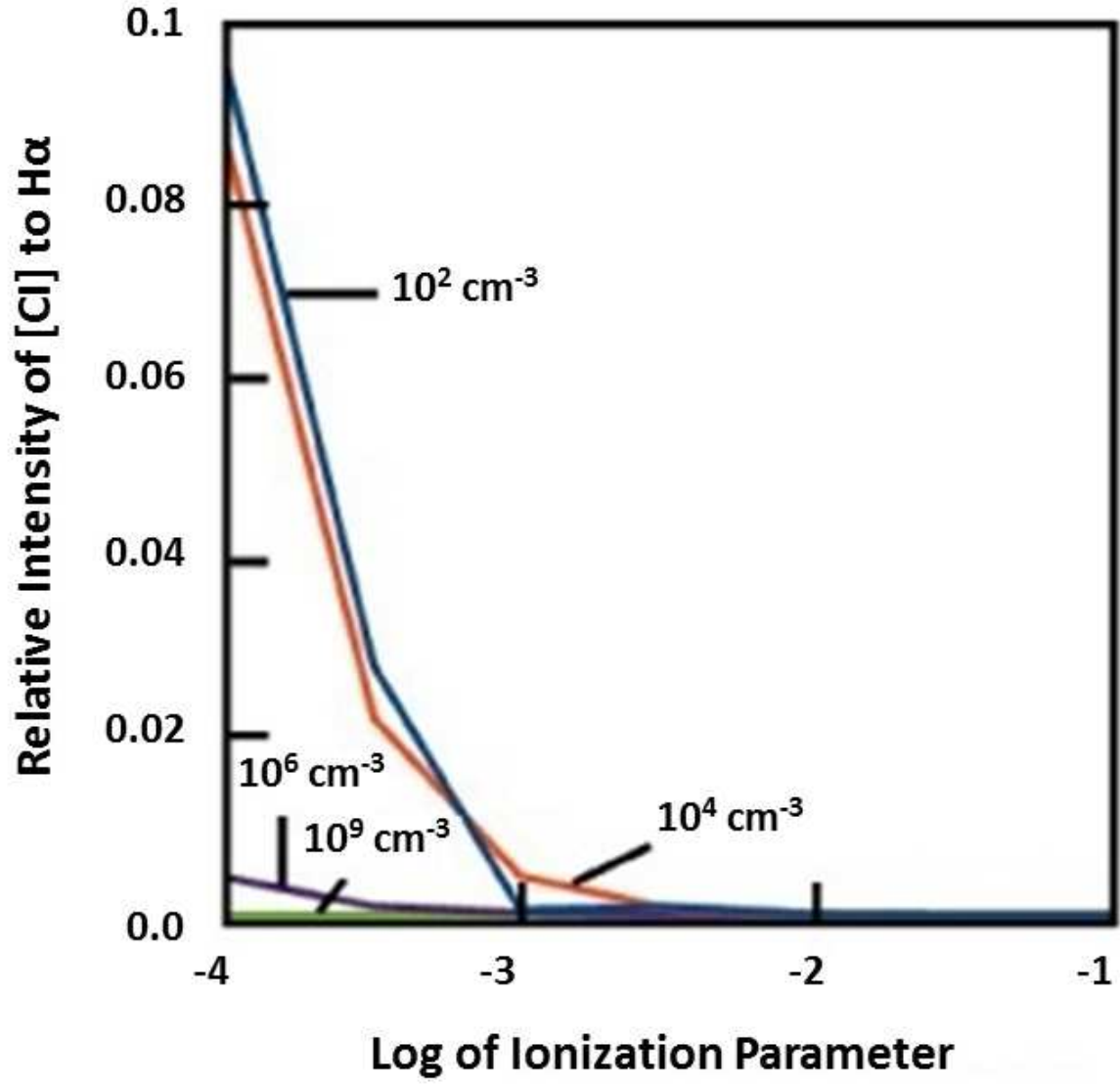


Fig. 10.— Computed [C I] $\lambda\lambda 9823,9850$ to $H\alpha$ ratio as functions of log ionization parameter and line-emitting gas density (cm^{-3}). For solar element abundances.